

Impact of the Substrate Material on the RF Performance of Carbon-Nanotube Transistors

Sabbir Ahmed, Navid Paydavosi, Ahsan UI Alam, Kyle David Holland, Diego Kienle,
and Mani Vaidyanathan, *Member, IEEE*

Abstract—We examine the effect of the substrate material on the radio-frequency (RF) behavior of carbon-nanotube transistors by considering the impact of substrate polar phonons (SPPs). We consider SPP scattering from AlN, SiO₂, HfO₂, and ZrO₂ substrates within a semiclassical approach by solving the time-dependent Boltzmann transport equation self-consistently with the Poisson equation. Various RF figures of merit, such as the unity-current gain frequency f_T , the unity-power-gain frequency f_{max} , the transconductance g_m , and the two-port y -parameters, are determined in order to characterize the impact of SPP scattering. We first consider the impact of SPP scattering on the RF behavior of an intrinsic single-tube carbon nanotube field-effect transistor (CNFET). These single-tube results are then combined with the external parasitic elements to analyze the pitch-dependent, RF behavior of an extrinsic array-based CNFET. It is shown that AlN substrates have the least impact in degrading the RF performance of a CNFET, while the more polar substrates (HfO₂ or ZrO₂) have a greater impact. This varying behavior can be attributed to the SPP energies, which are higher in AlN compared to the other materials, making CNFETs with AlN substrates less susceptible to SPP scattering even at room temperature. Our results suggest that substrate engineering will become an important component in the design process of emerging devices to achieve an optimized RF performance.

Index Terms—Carbon nanotube (CN), RF CMOS, high-frequency behavior, phonon scattering, radio-frequency (RF) behavior, substrate polar phonon (SPP), time-dependent transport, tube pitch, two-port parameters.

I. INTRODUCTION

SINCE their discovery in 1991, carbon nanotubes (CNs) have stimulated a plethora of experimental and theoretical research to better understand the charge transport in (quasi) 1-D-material systems, and to assess whether CN-based channel

Manuscript received May 6, 2013; accepted October 15, 2013. Date of publication December 11, 2013; date of current version January 6, 2014. This work was supported by the Natural Sciences and Engineering Research Council (NSERC) of Canada, Queen Elizabeth II Graduate Scholarship, and Alberta Advanced Education & Technology. The review of this paper was arranged by Associate Editor A. Ghosh.

S. Ahmed, A. U. Alam, K. D. Holland & M. Vaidyanathan are with the Department of Electrical and Computer Engineering, University of Alberta, Edmonton, AB, Canada (e-mail: maniv@ualberta.ca).

N. Paydavosi is with the BSIM Group, University of California, Berkeley, CA 94720, USA.

D. Kienle is with the Theoretische Physik I, Universität Bayreuth, D-Bayreuth, Germany.

Color versions of one or more of the figures in this paper are available online at <http://ieeexplore.ieee.org>.

Digital Object Identifier 10.1109/TNANO.2013.2294472

materials have the potential to replace or augment the well-matured, silicon-based CMOS technology [1].

One of the major concerns has been to understand how scattering by lattice vibrations *native* to the nanotube (native phonons) affect the terminal behavior of CN field-effect transistors (CNFETs). So far, most studies on native phonon scattering have been conducted for CNFETs under steady-state (dc) operating conditions [2]–[9]; both measurements and simulations of the dc mobility and output currents have revealed that native acoustic and optical phonons strongly contribute to limiting the transport in metallic and semiconducting tubes, including a saturation of the output current at high bias [2], [6], [10].

Another source of scattering (over and above that from native phonons) originates from phonons within the substrate on which the tube resides, and this has received detailed attention only recently, when it was realized that transport in nanoscale channels may be quite sensitive to the substrate type [11]–[13]. Many of these substrates are *polar* in nature, so that the lattice vibrations of the substrate form oscillating bond dipoles that generate polarization fields that die out exponentially from the surface [14]. In carbon-based materials, such as CNs and graphene, the distance between the atomically thin channel and the substrate is within 0.35 nm (Van-der Waals distance), and the polarization fields can interact quite strongly with the channel electrons, leading to the so-called “substrate polar phonon (SPP) scattering” [11]. It has been argued that beyond a temperature of $T = 100$ K, SPP scattering is activated and dominates the electronic transport, causing the dc mobility to degrade by a factor of 10 [15].

Regarding the radio-frequency (RF) behavior, recent studies have shown that CNFETs have the potential to outperform other high-frequency transistors, even in the presence of significant scattering from native acoustic and optical phonons [16]. However, this outcome should be revisited, given that SPP scattering has been flagged as an additional major contributor to device degradation at ambient temperatures [15]. As far as we know, a detailed investigation of the importance of SPP scattering on the RF performance of CNFETs has yet to be performed, either theoretically or experimentally.

In this paper, we investigate the impact of SPP scattering on the high-frequency characteristics of array-based, CN transistors at varying tube pitches. The RF performance is compared for four substrate materials: AlN, SiO₂, HfO₂, and ZrO₂. We show that SPP scattering substantially affects the device’s RF performance and, most importantly, displays a strong dependence on the choice of substrate. Among the materials studied, it is demonstrated that AlN degrades the device’s RF

performance the least, which can be attributed to the high energy of the phonons in AlN in comparison to the other substrates. This result is in accord with the qualitative expectation of Perebeinos *et al.* [15], who commented on the possible impact of different polar substrates on the dc mobility; in this paper, we focus on the RF performance, and we provide detailed quantitative results.

The simulation approach that allows us to extract the relevant RF figures of merit in the presence of various scattering sources consists of two steps. First, a solver for the time-dependent Boltzmann transport equation (BTE) self-consistently coupled to the Poisson equation, developed in [10] using COMSOL [17], is employed to simulate the RF behavior of an *intrinsic* single-tube device at various widths (pitches) of the tube block. The collision integrals for the SPP scattering, based on the formalism of [15], are developed and included in the BTE along with the collision integrals for the native acoustic and optical phonons. Second, the external parasitic resistances and capacitances are combined with the results of the intrinsic single-tube block as described in [16] to establish the *extrinsic* y -parameters of the array-based structure; these allow the extraction of key extrinsic high-frequency figures of merit, including the unity-current-gain frequency f_T , the unity-power-gain frequency f_{max} , the unilateral power gain U , the maximum stable gain (MSG), and the maximum available gain (MAG) [18].

This paper is organized as follows. Section II briefly summarizes the BTE-Poisson approach used to determine the RF transport characteristics of a single-tube block, including the scattering due to native acoustic, native optical, and substrate phonons; the details on the respective collision integrals are provided in the Appendix. We then proceed to determine the intrinsic high-frequency characteristics of a single-tube CNFET and to examine how these characteristics are impacted by the choice of substrate. In Section III, a complete lumped circuit model is developed for an overall array-based CNFET, that includes all parasitic elements, and we discuss how SPP scattering from different substrates affects the transistor's extrinsic RF figures of merit at various tube densities. The results of our investigation are summarized in Section IV.

II. INTRINSIC DEVICE

A. BTE-Poisson Approach

Fig. 1 shows the base geometry of the single-tube transistor used in the simulations, which consists of a semiconducting (16, 0) zigzag CN with a tube diameter $d = 1.25$ nm and a bandgap of $E_g = 0.55$ eV. The 50-nm-long source and drain contact regions are doped n -type, each at a level of 10^9 m^{-1} . The nanotube channel region underneath the gate is undoped and has a length of 20 nm in correspondence to the ITRS requirements for the year 2015 for RF CMOS millimeter-wave (10–100 GHz) technology [19]; HfO_2 is used as the gate oxide with an effective thickness (from the gate metal to the surface of the tube) of ~ 2 nm; the gate metal has a thickness of 50 nm and a work function of 4.5 eV, a typical value for W or Cr ; the tube resides on a 100-nm thick substrate consisting of different polar materials, as detailed further below. Varying the width of the base structure in Fig. 1 is equivalent to varying the tube pitch of an array

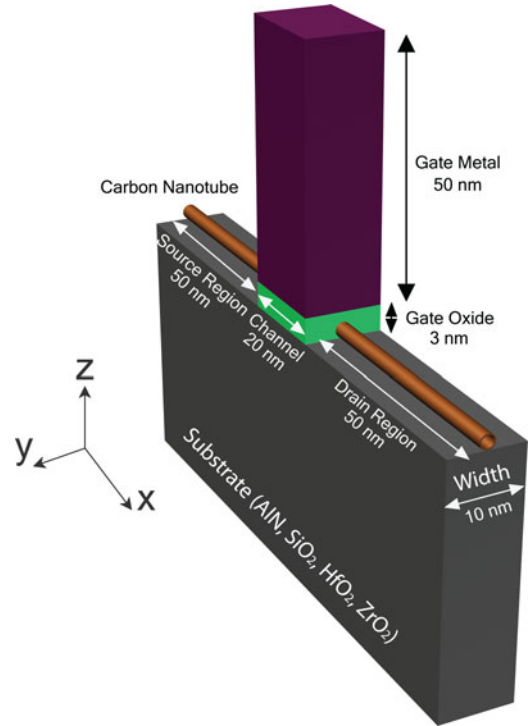


Fig. 1. Base geometry of the intrinsic single-tube CNFET structure used for the simulation.

containing the block, as explained in Section III-A-1. Block widths and hence array pitches of 10 and 100 nm correspond to 100 and 10 tubes, respectively, across a 1- μ m-wide, array-based device, which we use for demonstration purposes in this paper.

The electron dynamics within the tube is described by a one-dimensional (1D) BTE for the time-dependent distribution function $f = f(x, k, t)$ for electrons within the lowest conduction subband

$$\frac{\partial f}{\partial t} + v(k) \frac{\partial f}{\partial x} - \frac{q\varepsilon_x}{\hbar} \frac{\partial f}{\partial k} = S_o f \quad (1)$$

where the symbols are as follows: t is the time; k is the electron wave vector; $v(k)$ is the band velocity for an electron in a state k , obtained from $v(k) = (1/\hbar)[dE(k)/dk]$, with $E(k)$ being the band dispersion, given by [20, Eq. (6.1.12)]; $\varepsilon_x = \varepsilon_x(x, t)$ is the time-dependent, circumferentially averaged x -component of the electric field along the tube surface; q is the magnitude of the electronic charge; \hbar is the reduced Planck constant; and $S_o f$ denotes the total collision integral comprising all electronic scattering contributions, including acoustic $(S_o f)_{ac}$, optical $(S_o f)_{op}$, and SPPs $(S_o f)_{spp, \nu}$, as specified in the Appendix.

As detailed in the Appendix, we follow the “unscreened” approach of Perebeinos *et al.* [15] in formulating the SPP collision integrals, *i.e.*, we ignore the impact of “screening” as modeled by a Thomas–Fermi screening length [21], [22] or as determined by the coupling of the channel charge to the substrate phonons, where the latter leads to so-called “hybridized, interfacial plasmon–phonon (IPP) modes” [23]–[25]. While such screening may play an important role in 2-D/3-D materials, its significance in quasi-1-D systems such as CNs appears less severe [26]. We also note that our results with regard to RF

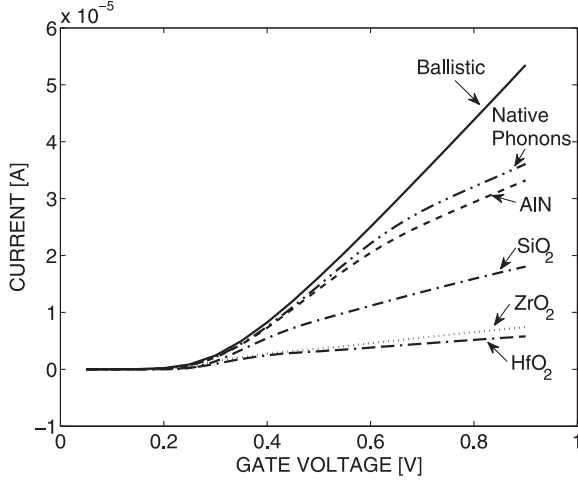


Fig. 2. Static (dc) drain current I_D versus gate bias voltage V_G for a single-tube block (shown in Fig. 1) with a tube pitch of 10 nm in the presence of SPP scattering on different substrates. The dc drain voltage V_D is held at 0.9 V. The curve labeled “Ballistic” is with all scattering turned off and the curve labeled “Native Phonons” includes scattering only from native acoustic and optical phonons; in each of these cases, an SiO_2 substrate is assumed solely for the purpose of solving Poisson’s equation (and with no contribution to the scattering). The remaining curves are for the indicated substrates with *all* scattering (native *and* SPP) turned on.

performance degradation in tubes (*e.g.*, see Figs. 2 and 3) are generally consistent in terms of the ordering of substrates (*e.g.*, AlN and SiO_2 versus HfO_2 and ZrO_2) with those found from a Thomas–Fermi approach for the dc mobility in 2-D graphene [22, Fig. 5], and that a Thomas–Fermi approach is generally in agreement with a fully coupled IPP approach [24, Fig. 3]. Thus, while it must be noted that the precise quantitative nature of our results may be impacted by a more detailed consideration of screening, for a first assessment of the relative importance of various substrates on the RF performance, we use the unscreened approach of [15].

To proceed, we make the usual assumption that a sinusoidal perturbation at a radian frequency ω is applied at one of the terminals, thus inducing a perturbation to the distribution function f and the electric field ε_x along the transport direction. For small signal amplitudes, both f and ε_x can be split into their dc and ac components via $f = \bar{f} + \tilde{f}e^{j\omega t}$ and $\varepsilon_x = \bar{\varepsilon}_x + \tilde{\varepsilon}_xe^{j\omega t}$, respectively, where here and elsewhere, we use the “ $\bar{\cdot}$ ” and “ $\tilde{\cdot}$ ” notation to distinguish between the dc and ac parts. Inserting this ansatz into (1), a BTE for each component can be derived following the approach of [10]:

$$v \frac{\partial \bar{f}}{\partial x} - \frac{q\bar{\varepsilon}_x}{\hbar} \frac{\partial \bar{f}}{\partial k} = S_o \bar{f} \quad (2)$$

$$j\omega \tilde{f} + v \frac{\partial \tilde{f}}{\partial x} - \frac{q\tilde{\varepsilon}_x}{\hbar} \frac{\partial \tilde{f}}{\partial k} - \frac{q\bar{\varepsilon}_x}{\hbar} \frac{\partial \tilde{f}}{\partial k} = S_o \{ \tilde{f}, \bar{f} \} \quad (3)$$

where $S_o \bar{f}$ and $S_o \{ \tilde{f}, \bar{f} \}$ refer to the total collision integrals applicable to the dc and ac equations, given by (9)–(11) with $f \rightarrow \bar{f}$ and by (14)–(16) in the Appendix, respectively.

The BTEs in (2) and (3) are solved self-consistently along with their corresponding Poisson equation, as described in [10]. All simulations are performed at room temperature $T = 300$ K.

B. Results for the Single Tube

1) *DC Output Current*: We begin our analysis by studying the effect of SPP scattering on the dc output characteristics of a single-tube block (see Fig. 1) with a width of 10 nm and a supply voltage of $V_D = V_{DD} = 0.9$ V, where the latter is consistent with the ITRS requirements for the year 2015 for RF CMOS millimeter-wave (10–100 GHz) technology [19].

Fig. 2 shows the dc drain current as a function of the gate bias V_G for a CNFET situated on different substrates. The curve labeled “Ballistic” is with all scattering turned off and the curve labeled “Native Phonons” includes scattering only from native acoustic and optical phonons; in each of these cases, an SiO_2 substrate is assumed solely for the purpose of solving Poisson’s equation (but with no contribution to the scattering). The remaining curves in Fig. 2 are for the indicated substrates with *all* scattering, *i.e.*, native *and* SPP, turned on. Starting with the ballistic limit, one observes a monotonic increase of the drain current with increasing gate bias. The inclusion of native acoustic and optical phonons leads to the expected reduction of current, which becomes pronounced at large V_G . The additional inclusion of SPP scattering causes a further reduction of the current, as depicted in Fig. 2, which for SiO_2 is about a factor of two at $V_G = 0.9$ V. What is striking is the strong dependence of the current on the type of substrate, as Fig. 2 demonstrates. Among all the substrates considered, AlN seems to play a distinguished role, since SPP scattering with AlN does not affect the device performance as severely as with the other substrates; for AlN, the drain current I_D is only slightly below that in the presence of only native phonon scattering.

The strong variation of the drain current with a change in substrate can be explained *in part* by the relative strengths of SPP scattering for the first ($\nu = 1$) substrate phonon mode, as indicated by the prefactor of the SPP collision integral specified in (11) of the Appendix; the role of the second ($\nu = 2$) substrate phonon mode, which corresponds to relatively higher values of phonon energy, requires a more careful consideration, as will be discussed shortly.

The prefactor $\text{PF}_{\text{spp},\nu}$ of the SPP collision integral in (11) can itself be written as a product of three factors:

$$\text{PF}_{\text{spp},\nu} = F_{\text{spp},\nu}^2 \times P_{\text{spp},\nu} \times (N_{\text{spp},\nu} + 1) \quad (4)$$

where the symbols are as follows: $F_{\text{spp},\nu}^2$ (known as the Fröhlich coupling) specifies the coupling strength between the electrons and the substrate phonons; $P_{\text{spp},\nu}$ is indicative of the strength of the polarization field due to the substrate phonons at a distance s away from the substrate, with a strong inverse dependence on the energy $\hbar\omega_{\text{spp},\nu}$ of the phonon mode, as indicated by an inspection of (12) and (13) in the Appendix; and $N_{\text{spp},\nu} = 1 / (e^{\hbar\omega_{\text{spp},\nu}/k_B T} - 1)$ is the number of substrate phonons, which also exhibits a strong inverse dependence on the energy $\hbar\omega_{\text{spp},\nu}$ of the phonon mode. As Table I reveals, the $\nu = 1$ modes have a similar electron–phonon coupling factor, $F_{\text{spp},1}^2 \sim 0.5 - 0.75 \text{ V}^2\text{m}$, while the phonon energies $\hbar\omega_{\text{spp},1}$ are well-ordered, from about 90 meV for AlN, 60 meV for SiO_2 , and 28 and 22 meV for ZrO_2 and HfO_2 , respectively. As the values in Table I show, the differences in these energies dominates

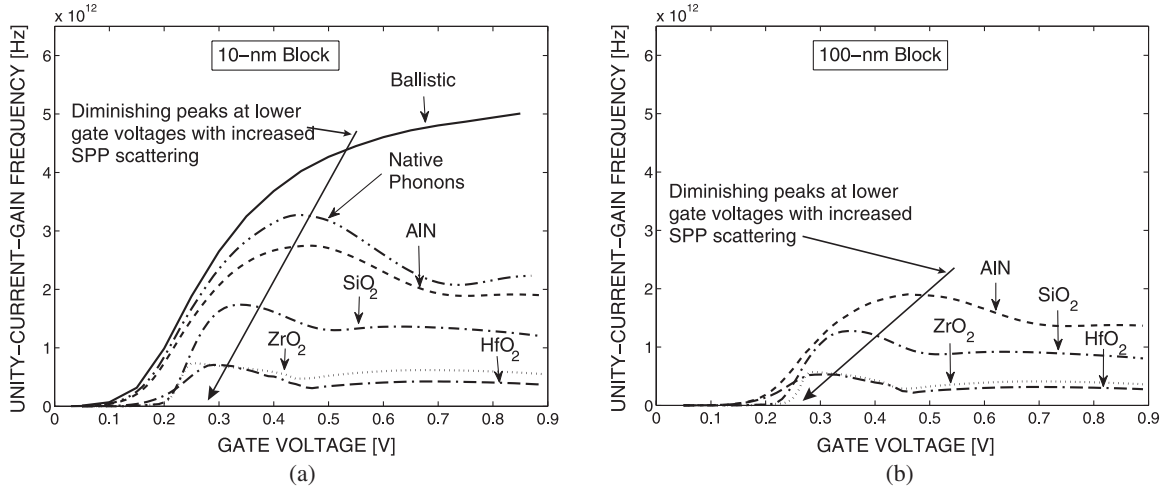


Fig. 3. Intrinsic unity-current-gain cutoff frequency f_T versus gate voltage V_G for the single-tube CNFET block shown in Fig. 1 and for block widths of (a) 10 nm and (b) 100 nm. The labeling convention for the curves is the same as that described in the caption of Fig. 2.

TABLE I
PARAMETERS FOR THE SPP SCATTERING IN CNS ON VARIOUS SUBSTRATES [27]

	AlN	SiO ₂	ZrO ₂	HfO ₂
ϵ^0	9.14	3.90	24.0	22.0
ϵ^∞	4.80	2.50	4.00	5.03
$\hbar\omega_{spp,1}$ [meV]	90	61	28	22
$F_{spp,1}^2 \times 10^{-11}$ [V ² m]	0.55	0.75	0.60	0.55
$P_{spp,1} \times 10^9$ [eV/V ² s]	0.67	0.97	1.95	2.44
$N_{spp,1} + 1$	1.03	1.09	1.48	1.73
$PF_{spp,1} \times 10^6$ [eVm/s]	0.21	0.44	0.96	1.29
$\hbar\omega_{spp,2}$ [meV]	106	149	76	54
$P_{spp,2} \times 10^9$ [eV/V ² s]	0.57	0.40	0.79	1.09
$F_{spp,2}^2 \times 10^{-11}$ [V ² m]	1.61	1.66	1.88	0.53
$N_{spp,2} + 1$	1.01	1.00	1.05	1.13
$PF_{spp,2} \times 10^6$ [eVm/s]	0.51	0.36	0.86	0.36
Peak f_T [THz]	2.75 - 1.90	1.74 - 1.27	0.73 - 0.57	0.71 - 0.53
V_G for peak f_T [V]	0.46 - 0.46	0.34 - 0.35	0.25 - 0.28	0.29 - 0.31

the collision-integral prefactor $PF_{spp,1}$, through the impact on the polarization factor $P_{spp,1}$ and phonon number ($N_{spp,1} + 1$), and this is especially true for ZrO₂ and HfO₂. Overall, and at least for the first phonon mode, the low-energy SPP phonons in ZrO₂ and HfO₂, and to a lesser extent SiO₂, can thus be expected to cause increased SPP scattering and hence a more severe degradation in the current, as demonstrated in Fig. 2.

For the second phonon mode, the situation is more involved, as one needs to consider more than simply the prefactor in the collision integral (11) in determining the relative strengths of the scattering. The higher phonon energies of the second mode suggest that the corresponding SPP scattering will become important only at higher gate biases, when the channel band profile has

been “pushed down” sufficiently below the source Fermi level for carriers injected from the source to have available states to occupy in the channel and in the channel-to-drain barrier region upon emitting the higher ($\nu = 2$) energy SPP phonons; mathematically, the requirement for available states is taken into account by the presence of the density of states and distribution function in the collision integral (11). Again, in this case, ZrO₂ and HfO₂ can be expected to suffer from more severe SPP scattering, *i.e.*, scattering that becomes important at a lower gate voltage, since $\hbar\omega_{spp,2}$ is significantly lower for these materials, thus requiring less gate voltage to push the bands down a sufficient amount. The curves in Fig. 2 are indeed consistent with this expectation.

Overall, considering both substrate phonon modes, the important conclusion is that the lower substrate phonon energies ($\hbar\omega_{spp,1}$ and $\hbar\omega_{spp,2}$ in Table I) in ZrO₂ and HfO₂, and to a lesser extent SiO₂, lead to a greater degradation of the current than in AlN.

2) Cutoff Frequency:

a) *Results:* Over and above the dc current-voltage behavior, SPP scattering also has a strong impact on the device’s RF figures of merit, such as the unity-current-gain, cutoff frequency $f_T = g_m / (2\pi C_{gg})$, where g_m is the transconductance and C_{gg} is the total gate capacitance.

Fig. 3 shows the f_T versus gate bias V_G for the same cases (and with the same labeling convention) as in Fig. 2, but for two different single-tube block widths of 10 and 100 nm. First focusing on the curves for a 10-nm block width [part (a) of Fig. 3], a distinct pattern in the behavior of f_T versus V_G is evident. In the ballistic case, the f_T exhibits a monotonic increase with V_G , before saturating at high values of V_G . In the presence of native acoustic and optical phonon scattering, the f_T still increases monotonically with V_G at low gate bias, but then exhibits a clear peak before falling off and saturating at high gate bias. In the additional presence of SPP scattering, the peaking behavior is still present, but the peaks diminish and shift to lower gate voltages in an order corresponding to the expected strength of the SPP scattering as already discussed in conjunction with Fig. 2,

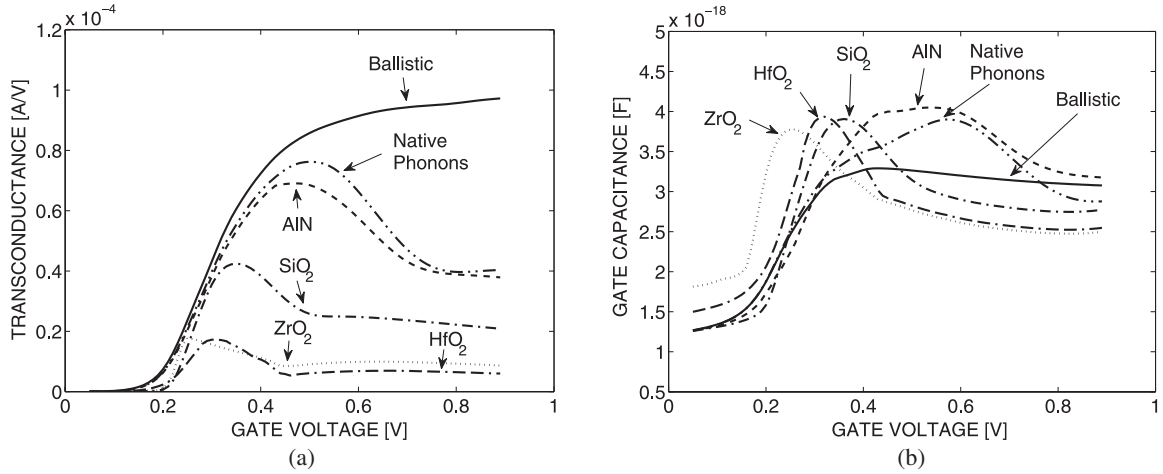


Fig. 4. (a) Transconductance g_m and (b) gate capacitance C_{gg} versus dc gate voltage V_G of a single-tube CNFET block in Fig. 1 with a width of 10 nm. The labeling convention for the curves is the same as that described in the caption of Fig. 1.

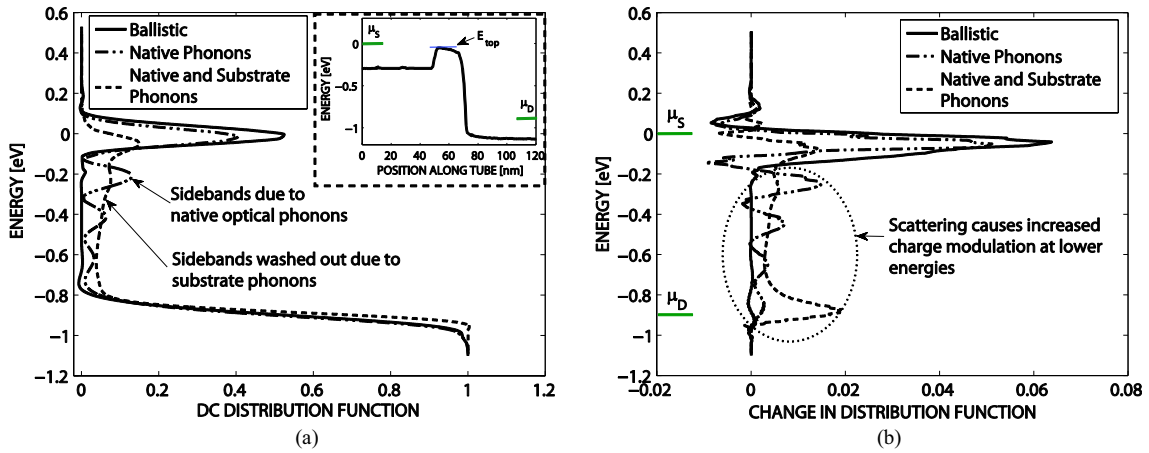


Fig. 5. (a) Energy-resolved dc distribution function $\bar{f}(E)$ at $x = 80$ nm (see Fig. 1) and for $V_G = 0.4$ V, with SiO_2 used as the substrate and shown for three cases: (i) ballistic transport; (ii) only native acoustic and optical phonon scattering; (iii) all scattering, *i.e.*, additionally including substrate phonons. The inset to the figure shows a sketch of the conduction-band profile $E_c(x)$ versus x , which is provided for reference. (b) Energy-resolved change in the distribution function $\Delta\bar{f}(E)$ at $x = 80$ nm and $V_G = 0.4$ V, where $\Delta\bar{f}(E)$ arises from an incremental change in gate voltage ΔV_G (equal to 10 mV).

i.e., starting from AlN (having high SPP phonon energies), followed by SiO_2 (with intermediate SPP phonon energies), and finally by ZrO_2 and HfO_2 (having low SPP phonon energies). In the case of the 100-nm block width [part (b) of Fig. 3], the behavior is similar, but the f_T values are lower, a result that will be explained in Section III-B-2. For reference, the peak f_T values and the gate bias V_G at which they occur for the different substrates are listed in Table I.

b) Discussion: One can understand the behavior of the f_T in Fig. 3 by considering separately the behavior of the g_m and C_{gg} , both of which are plotted versus gate bias V_G in Fig. 4; we restrict our attention in this discussion to the case of a 10-nm block width.

The transconductance $g_m = \partial I_D / \partial V_G$ in Fig. 4(a) represents the local slope of the $I_D - V_G$ characteristics, and hence peaks at the point of inflection of the corresponding $I_D - V_G$ curve in Fig. 2. Based on the earlier discussion of the $I_D - V_G$ curves, the peaks in g_m are hence diminished and occur at successively lower gate voltages with increased scattering, and this behavior

is primarily responsible for the peaking pattern of the f_T in Fig. 3. However, C_{gg} also plays a role, accentuating the peaking in f_T by itself peaking, as shown in Fig. 4(b). These peaks in C_{gg} are worth a more careful consideration.

Fig. 5(a) shows a plot of the energy-resolved dc charge distribution $\bar{f}(E)$ for the case of SiO_2 as the substrate; we choose a bias point of $V_G = 0.4$ V for illustration, and we choose to plot the distribution at the point $x = 80$ nm (see Fig. 1), which is just past the channel region and where the effects of scattering (when present) are clearly visible. The plot shows $\bar{f}(E)$ for three cases: (i) ballistic transport, (ii) with only native acoustic and optical phonon scattering, and (iii) with all scattering, *i.e.*, by additionally including SPP phonons. In the ballistic case, $\bar{f}(E)$ shows the expected peak for energies above the top of the barrier and below the source Fermi level ($E_{\text{top}} \lesssim E \lesssim \mu_S$), representing source-injected electrons that can cross the channel barrier; $\bar{f}(E)$ is otherwise zero except for energies around the drain Fermi level ($E \sim \mu_D$), representing drain-injected electrons. In

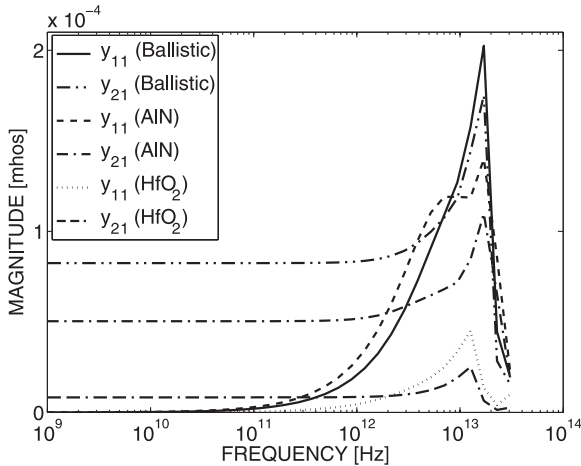


Fig. 6. Magnitude of the transistor's forward y -parameters, y_{11} and y_{21} , comparing the ballistic limit with the case of SPP scattering for the two substrates AlN and HfO₂, where the SPP scattering is the weakest and strongest, respectively.

the presence of only native acoustic and optical phonon scattering, the distribution function takes a similar shape, except now we see “sidebands” of occupancy facilitated by optical phonon emissions; carriers are moved down from the ballistic peak in bands separated by the optical phonon energy of $\hbar\omega_{\text{op}} = 200$ meV [2]. With the addition of SPPs, the signature of the native optical phonon sidebands is “washed out” because the SPPs allow transitions over additional energies (specified by the values of $\hbar\omega_{\text{spp},1}$ and $\hbar\omega_{\text{spp},2}$ in Table I). The important point to note is that *scattering moves carriers from the ballistic peak down to lower energies*. As a result, with scattering, a perturbation in gate voltage ΔV_G leads to a modulation of the distribution function $\Delta \bar{f}(E)$ at energies below the ballistic peak, as shown in Fig. 5(b); overall, the additional modulation at lower energies more than compensates the decreased modulation in the ballistic peak, such that the integrated charge modulation $\Delta Q_G \approx q \int_{\mu_D}^{\mu_S} [\Delta \bar{f}(E) \times D(E)] dE$ is higher in the presence of increased scattering,¹ which will tend to increase the capacitance $C_{\text{gg}} \sim \Delta Q_G / \Delta V_G$ seen looking into the gate. The effect is most pronounced at the gate bias corresponding to the onset of scattering, since the lower energy states fill up at higher gate biases, thereby causing increased Pauli blocking and hence a reduced modulation; this is why the capacitance peaks at the onset of scattering in Fig. 4(b).

3) y -Parameters: We conclude our analysis of the RF behavior of the single-tube block by extracting its frequency-dependent y -parameters from our self-consistent BTE-Poisson solution, as described in [10]. Fig. 6 shows the magnitude of the transistor's intrinsic forward y -parameters, y_{11} and y_{12} , for the single-tube block of Fig. 1 having a width of 10 nm; results are shown for a ballistic device and a device with all scattering, *i.e.*, due to native acoustic and optical phonons as well as substrate phonons. The ballistic device is again assumed to lie on a SiO₂

¹Here, we have used $\Delta \bar{f}(E) \approx 0$ outside the interval of integration and the fact that $D(E)$ [given by (8) in the Appendix] decreases monotonically with energy.

substrate, solely for the purpose of solving Poisson's equation. For the devices with all scattering included, the focus is on the choice of AlN and HfO₂ as substrates, *i.e.*, the materials where the signatures of scattering are the weakest and strongest, respectively. For the ballistic case, the operating bias is chosen to be equal to $V_G = V_{\text{DD}}/2$ as in [10], and for the cases with scattering, V_G is chosen to be the gate voltage corresponding to peak f_T , which is 0.46 V for AlN and 0.29 V for HfO₂; in all cases, the drain voltage is held fixed at 0.9 V.

As Fig. 6 reveals, scattering lowers the forward y -parameters for both AlN and HfO₂ over the entire frequency range. Despite the strong impact of the SPP phonons, one still observes a resonant behavior at about the same frequency of approximately 18 THz. This resonant behavior has been discussed in [10], [28]–[31]. Compared to the ballistic case, the resonances are not only lowered but also strongly broadened due to scattering, which is equivalent to a reduction in the quality (Q) factor. As Fig. 6 shows, the degradation in the y -parameters is more severe for HfO₂ than for AlN since, as discussed earlier, SPP scattering has a stronger impact (due to the lower phonon energies) in HfO₂ than AlN.

III. EXTRINSIC DEVICE

A. Approach

1) *Array-Based Structure*: A schematic of the multitube CNFET structure used in this paper is shown in Fig. 7, and it consists of a parallel arrangement of the single-tube blocks from Fig. 1; the total width of the device in the y -direction, *i.e.*, the gate width, is fixed to be $W_g = 1 \mu\text{m}$, and the distance between the tubes, *i.e.*, the tube pitch p , is varied between 10 and 100 nm, corresponding to a total of 100 and 10 tubes, respectively. Here, it is important to note that the pitch p of the array in Fig. 7 is equivalent to the width of a single-tube block in Fig. 1; this follows since the block of Fig. 1 can represent a portion of an array when the appropriate boundary conditions are applied at the edges (along the tube length) of the block [32], which is what we have done throughout this paper. The *intrinsic* y -parameters of the multitube array, *i.e.*, *excluding parasitics*, can be found by a scaling of the intrinsic y -parameters of a single-tube block; for our 1- μm wide transistor, we can write [16]

$$[y_{\text{m,int}}]_p = [y_{\text{s,int}}]_p \times \left(\frac{1000 [\text{nm}]}{p [\text{nm}]} \right) \quad (5)$$

where $[y_{\text{m,int}}]_p$ and $[y_{\text{s,int}}]_p$ denote the y -parameter matrices of the multi and single-tube structures, respectively; both matrices are functions of the tube pitch p .

2) *Modeling of Parasitics*: A major cause for the overall performance degradation of the device is the impact of the extrinsic capacitances and resistances originating from the contacts, which makes it necessary to incorporate these into a complete device model, as shown in Fig. 8. To determine the values of these external elements, we follow the procedure explained in [16], utilizing COMSOL [17]; for the details, including the choice of materials and dimensions of the contacts, the reader is referred to [16], and here we simply list the extracted values in Table II.

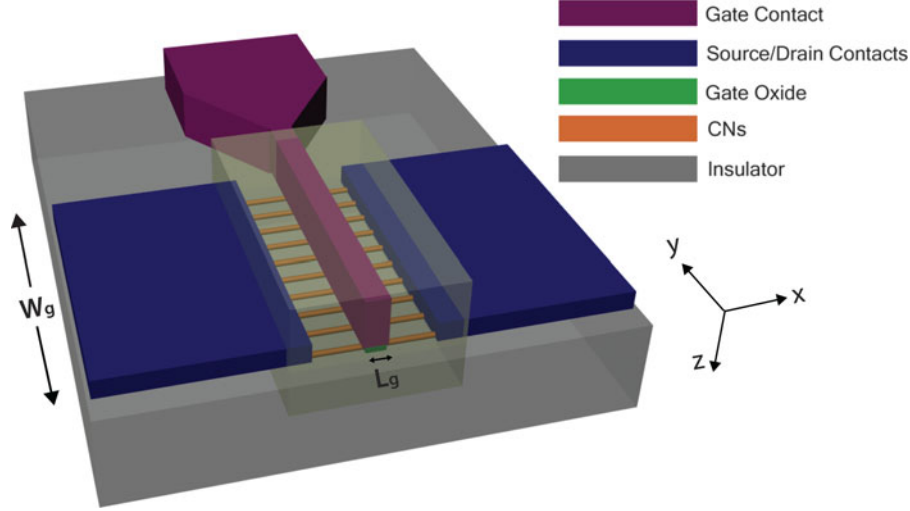


Fig. 7. Schematic of a top-gated, aligned, array-based CNFET structure similar to [16]. The gate length and width of the device are $L_g = 20$ nm and $W_g = 1$ μ m, respectively. The yellow box shows the portion of the structure that is studied. The figure is not drawn to scale.

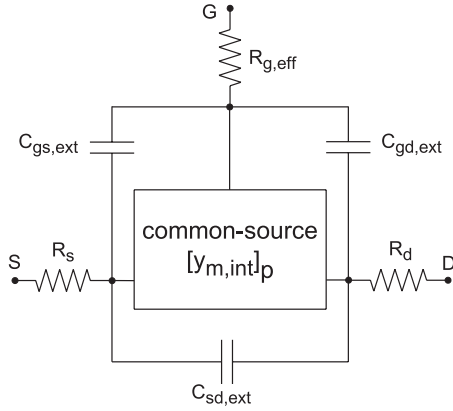


Fig. 8. Extrinsic lumped-element model of the array-based CNFET structure [16]. The inner block represents the intrinsic multitube device described by the y -parameter matrix $[y_{m,int}]_p$ specified by (5).

TABLE II
VALUES FOR THE PARASITIC RESISTANCES AND CAPACITANCES USED IN THE LUMPED ELEMENT MODEL OF FIG. 8 FOR THE DIFFERENT SUBSTRATES

	AlN	SiO ₂	ZrO ₂	HfO ₂
$R_{g,eff}$ (Ω) (Tungsten)	67	67	67	67
$R_{s/d}$ (Ω) (Yttrium)	1.77	1.77	1.77	1.77
$C_{gs,ext}$ (aF)	34	22	70	51
$C_{gd,ext}$ (aF)	32	21	66	48
$C_{sd,ext}$ (aF)	9.7	4.7	29	18

In all cases, the total width of the array-based CNFET is 1 micron.

B. Results and Discussion

1) *RF Figures of Merit*: Fig. 9 shows the extrinsic common-source current gain $|h_{21}| = |y_{21}/y_{11}|$ versus frequency and the extrinsic cutoff frequency f_T for a 1- μ m-wide, array-based structure with a pitch $p = 10$ nm; here and for all the extrinsic results, the operating bias is chosen to be the gate voltage

corresponding to peak intrinsic f_T with the drain voltage held fixed at 0.9 V. Notably, despite the presence of SPP scattering, CNFETs with AlN substrates still offer the potential for an extrinsic f_T of about 2.43 THz, and thus remain ahead of the present records for RF transistors reported in the literature, which include graphene transistors with 300 GHz [33], silicon MOSFETs with 485 GHz [34], III-V high-electron mobility transistors with 644 GHz [35], and heterojunction bipolar transistors with 710 GHz [36]. However, this is no longer the case for a substrate leading to strong SPP scattering, such as HfO₂, where the extrinsic f_T falls to 470 GHz, comparable to silicon MOSFETs.

Other RF measures to characterize the device are also shown in Fig. 9, such as the unilateral power gain U , the MSG, the MAG, and the Kurokawa stability factor \mathbf{k} [37]; all figures of merit are calculated based on well-known expressions [37] using the y -parameters extracted from the extrinsic device model shown in Fig. 8. Similar to [10], the MSG is plotted for those frequencies where the transistor is conditionally stable ($\mathbf{k} < 1$) and is replaced by the MAG when the device becomes unconditionally stable ($\mathbf{k} \geq 1$) [37]. Extrapolating the power-gain U to unity, the f_{max} can be extracted to be 3.24 THz for AlN and a lower value of 1.42 THz for HfO₂, where the SPP scattering is stronger.

2) Effect of Pitch on f_T and f_{max} :

a) *Unity-Current-Gain Frequency f_T* : Fig. 10 shows the extrinsic f_T as a function of the tube pitch in the presence of native and SPP scattering from the various substrates. As shown, the f_T can be improved by a factor of about 2.5 to 3.5 by decreasing the pitch from 100 to 10 nm. One can understand the improvement by considering that the pitch dependence of the extrinsic f_T is determined by the pitch dependence of the intrinsic transconductance and gate capacitance of the multitube system (neglecting parasitics), both of which are given by the single-tube values multiplied by the number of tubes N : $g_{m,int}^m|_p = N \times g_{m,int}^s|_p$ and $C_{gg,int}^m|_p = N \times C_{gg,int}^s|_p$, where the superscripts m and s refer to “multitube” and “single-tube,”

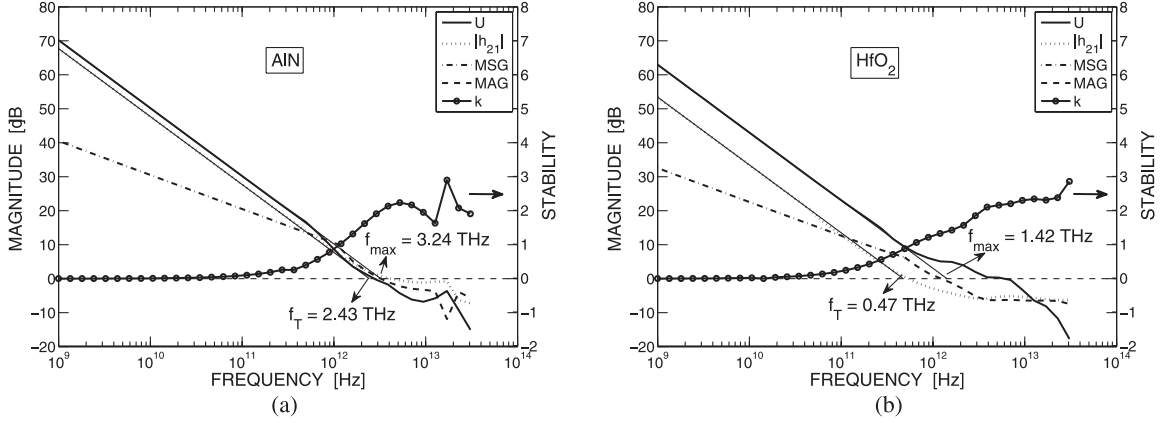


Fig. 9. Magnitude of the common-source current gain $|h_{21}|$, unilateral power gain U , MSG, MAG, and the stability factor k as function of frequency for the CNFET of Fig. 7 with a tube pitch $p = 10$ nm and with (a) AlN and (b) HfO₂ as substrates. The extrapolated f_T and f_{max} are also shown.

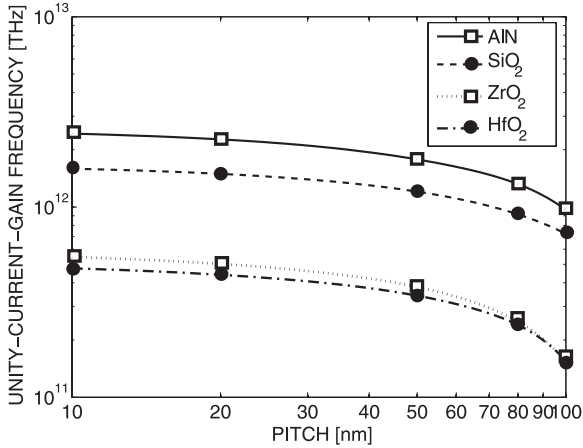


Fig. 10. Extrapolated extrinsic f_T of the array-based CNFET structure as a function of tube pitch in the presence of native and SPP scattering for different substrates.

respectively, and where the notation “ $|_p$ ” is used to emphasize that the corresponding quantities depend on the tube pitch p . To first order, we can estimate the pitch dependence by writing the extrinsic $f_T \sim g_{m,int}^m |p / C_{gg,int}^m |p = g_{m,int}^s |p / C_{gg,int}^s |p$. With a decrease in pitch (higher tube density), both $g_{m,int}^s |p$ and $C_{gg,int}^s |p$ decrease due to tube screening [32]; the important point is that $C_{gg,int}^s |p$ decreases by 30–35% (depending on the substrate) whereas $g_{m,int}^s |p$ reduces by only 3–7% when the pitch is scaled down from 100 to 10 nm (not shown). This difference in reduction results in an effective increase of the f_T as reported in [32] and as depicted in Fig. 10; it also explains why the f_T results for the 10-nm block presented earlier in Fig. 3(a) exceed those for the 100-nm block in Fig. 3(b). More importantly, Fig. 10 shows that the RF performance advantage of an AlN substrate continues to exist for the *extrinsic* cutoff frequency f_T , a consequence of AlN’s high-energy SPP phonons causing weaker SPP scattering as compared to HfO₂ and ZrO₂ substrates, as discussed earlier in Section II.

b) Unity-Power-Gain Frequency f_{max} : Contrary to the f_T , the transistor’s f_{max} is much less susceptible to variations of the tube pitch; for example, it grows by a factor of about 1.2

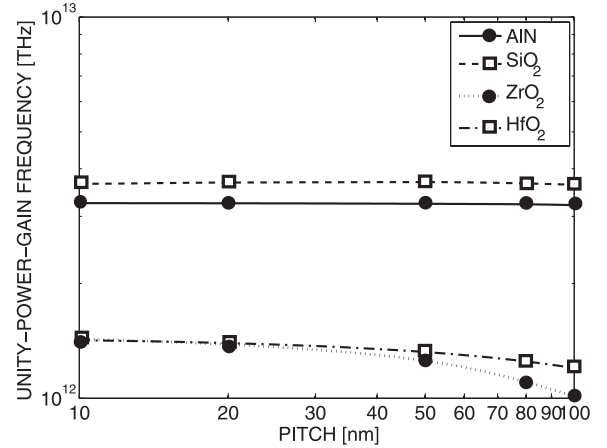


Fig. 11. f_{max} of the array-based CNFET structure as function of tube pitch in the presence of native and SPP scattering for different substrates.

to 1.5 for the HfO₂ and ZrO₂ substrates and not at all for SiO₂ and AlN when the pitch is decreased from 100 to 10 nm, as can be discerned from Fig. 11. This behavior of the f_{max} can be explained with the aid of the approximate expression [38], [39]

$$f_{max} \approx \sqrt{\frac{f_T}{8\pi R_{g,eff} C_{gd,eff}}} \quad (6)$$

which has been shown to reproduce the pitch-dependence of the numerically obtained f_{max} quite well [16]. Here, $R_{g,eff}$ is the effective gate resistance (shown in Fig. 8) and $C_{gd,eff}$ is the total effective gate-drain capacitance, which can be expressed as [16]

$$C_{gd,eff} = N \times C_{gd,int}^s |p + C_{gd,ext} \quad (7)$$

where $C_{gd,int}^s |p$ refers to the gate-drain capacitance of the intrinsic single-tube CNFET block of Fig. 1, and $C_{gd,ext}$ is the external gate-drain capacitance of the array-based CNFET shown in Fig. 6 and listed in Table II. Decreasing the pitch corresponds to a larger N , causing the term $N \times C_{gd,int}^s |p$ and thus $C_{gd,eff}$ to grow, as Fig. 12 shows; this increase of $C_{gd,eff}$ compensates the increase of the f_T discussed in conjunction with Fig. 10, causing the f_{max} to remain almost unaffected from a variation of the pitch [16].

TABLE III
ITRS RF CMOS MILLIMETER-WAVE TECHNOLOGY REQUIREMENTS FOR THE YEAR 2015 [19] VERSUS THE ARRAY-BASED CNFET WITH SPP SCATTERING INCLUDED FROM VARIOUS POLAR SUBSTRATES

	Power Supply Voltage V_{DD} [V]	Gate Length L_g [nm]	Peak f_T [THz]	Peak f_{max} [THz]	Peak g_m at $V_{DS}=V_{DD}$ [S/mm]	MSG/MAG [dB] at 24 GHz	MSG/MAG [dB] at 60 GHz	MSG/MAG [dB] at 94 GHz	
Array-Based CNFET Gate Width $1\mu\text{m}$ [10]	0.9	20	1.29	4.77	0.78	22	18	16	
Array-Based CNFET with SPP scattering (This Study)	AlN	0.9	20	0.96	3.21	0.74	19	16	13
	SiO ₂	0.9	20	0.72	3.63	0.44	19	15	12
	ZrO ₂	0.9	20	0.15	1.01	0.20	11	8	5
	HfO ₂	0.9	20	0.16	1.20	0.18	12	9	7
RF CMOS (ITRS)	0.9	20	0.44	0.56	2.24	17.4	13.4	11.5	

The tube pitch is 100nm.

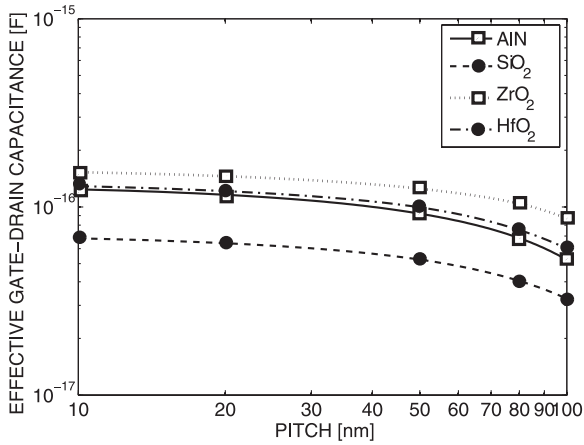


Fig. 12. Effective gate-drain capacitance $C_{gd,eff}$ for the array-based CNFET structure as a function of tube pitch in the presence of native and SPP scattering from different substrates.

Another interesting feature of Fig. 11 is that the f_{max} for SiO₂ is slightly higher than for AlN at all tube pitches, despite the lower f_T for SiO₂ in Fig. 10. The reason for the higher f_{max} of SiO₂-based CNFETs is due to the relative permittivity of SiO₂, which at 3.9 is the lowest among all substrates, as seen from Table I. The low permittivity causes the external parasitic capacitance $C_{gd,ext}$ for SiO₂ to be the smallest, which translates into the smallest overall $C_{gd,eff}$, as shown in Fig. 12; owing to the inverse dependence of the f_{max} on $C_{gd,eff}$ according to (6), CNFETs with SiO₂ rather than AlN substrates thus have a slightly higher f_{max} at all tube pitches. In the case of HfO₂ and ZrO₂, which have already been flagged as the worst for RF performance due to strong SPP scattering, the relatively higher values of the dielectric permittivity (see Table I) add to the degradation of f_{max} due to a larger $C_{gd,eff}$.

It should be noted that the results here (and throughout this paper) assume room temperature operation. Self-heating has been experimentally observed at small gate lengths, which could potentially increase the operating temperature and impact the device behavior, especially at high drive currents [2], [40]. For simplicity, and for a first assessment, we omit self-heating effects in our study; this assumes good heat removal and is consistent with our assumption [see the Appendix] of including only phonon emission processes.

c) Summary: In Table III, we summarize and compare the RF figures of merit for the array-based CNFET with the ITRS RF CMOS millimeter-wave technology requirements for the year 2015 [19]. Note that the reported values for the array-based CNFET are for a tube pitch of 100 nm, and can be improved by increasing the tube density as discussed in the previous sections; included also are the transistor's gain at frequencies of 24, 60, and 94 GHz, since these are of commercial interest [19]. As shown in Table III, despite the presence of SPP scattering (over and above native acoustic and optical phonons), and except for the transconductance g_m (which could be improved with a lower tube pitch than the assumed 100 nm), array-based CNFETs with AlN and SiO₂ substrates continue to offer performance that meets and exceeds the ITRS specifications for RF CMOS.

IV. CONCLUSION

The following conclusions can be drawn from this study of the impact of the substrate material via SPP scattering on the RF performance of array-based, CN transistors:

- 1) Scattering due to surface polar phonons, modeled according to the approach of [15], causes a significant reduction of the transistor's RF performance (see Figs. 3, 10, and 11) compared to a ballistic device; the magnitude of this reduction depends strongly on the substrate.
- 2) Among the materials considered in this work, AlN leads to the weakest impact of SPP scattering on the performance degradation; this can be attributed to the high energies of the excited SPP modes of AlN. On the other hand, the substrate phonon energies of HfO₂ and ZrO₂ are rather low, leading to strong SPP scattering and thus to a severe RF performance degradation, which becomes evident in a much lower cutoff frequency f_T (see Fig. 3). Another consequence of the disparity in the SPP phonon energies is that the f_T adopts its maximum at a larger gate bias V_G for AlN than for HfO₂ and ZrO₂ (see Fig. 3).
- 3) SPP scattering lowers the forward y -parameters over the entire frequency range, with the decrease becoming worse as the scattering gets stronger (see Fig. 6). In addition, SPP scattering causes the resonant behavior in the y -parameters [10], [28]–[31] to become smeared out (lower Q factor).
- 4) The extrinsic f_T increases by a factor of about two as the pitch is decreased from 100 to 10 nm (see Fig. 10).

The extrinsic f_T for AlN remains the largest for all the pitches since SPP scattering with AlN has the least impact on the RF degradation. Correspondingly, HfO₂ and ZrO₂ lead to the lowest extrinsic f_T as a result of their strong susceptibility to SPP scattering.

- 5) The extrinsic f_{\max} remains quite insensitive to pitch variations (see Fig. 11), which is a result of the increase in the effective gate-drain capacitance $C_{\text{gd,eff}}$ with decreasing pitch (see Fig. 12), thus counteracting the improvement of the extrinsic f_T . Due to the low dielectric permittivity (ϵ^0 in Table I) of SiO₂ substrates, the external parasitic capacitance $C_{\text{gd,ext}}$ and thus the $C_{\text{gd,eff}}$ is the smallest; as a consequence, the f_{\max} with an SiO₂ substrate becomes the largest for all pitches. On the other hand, ZrO₂ and HfO₂ suffer from a high dielectric permittivity leading to a large $C_{\text{gd,ext}}$, which tends to degrade the already poor f_{\max} arising from a low f_T with these substrates due to pronounced SPP scattering.
- 6) Despite the presence of SPP scattering (over and above native acoustic and optical phonons), and except for the transconductance g_m (which could be improved with a lower tube pitch), the results in Table III show that an array-based CNFET with a gate width of 1 μm , a gate length of 20 nm, and a tube pitch of 100 nm built on AlN and SiO₂ substrates continue to offer performance that meets and exceeds the ITRS specifications for RF CMOS [19]. The same is not true for HfO₂ and ZrO₂ substrates.

In summary, this paper shows that SPP scattering can significantly impact the RF performance of array-based CNFETs. Our reported findings may be experimentally probed by performing an RF characterization of array-based CNFETs fabricated on different substrates. More generally, our results suggest that substrate effects should be carefully considered to improve the performance of all future high-frequency devices; for example, similar results on the RF degradation could be expected for graphene-based FETs, since the distance between the substrate and channel material is comparable.

APPENDIX

In the following, we provide expressions for the full collision integrals appearing in the BTE transport equations (1)–(3) due to the scattering of electrons with native acoustic, native optical, and the ν th surface polar phonon modes, all of which can be calculated following the standard approach described in [41] and [10]. Similar to [10], only the process due to phonon emission is considered, in which case the collision integrals contain factors for the effective phonon occupancy of the form $(N_\gamma + 1)$, where $\gamma = \text{ac, op, or spp, } \nu$, corresponding to native acoustic, native optical, and the ν th surface polar phonon modes. At a given temperature T and phonon energy $\hbar\omega_\gamma$, this occupancy is given through the Bose–Einstein distribution, $N_\gamma = 1 / (e^{\hbar\omega_\gamma / k_B T} - 1)$, with k_B being Boltzmann’s constant. Another factor that determines the magnitude of the collision integral for each scattering process γ is how many states are available at a specific energy $E(k)$ for an electron in

a state k ; this information is contained in the density of states of the semiconducting nanotube,

$$D[E(k)] = \frac{8}{3\pi a_0 t_E} \frac{[E(k) + E_0]}{\sqrt{[E(k) + E_0]^2 - E_0^2}} \quad (8)$$

where $E_0 = E_g/2$ is half of the tube’s band gap.

A. Full Collision Integrals

1) *Acoustic Phonons*: The collision integral for acoustic phonons can be represented as

$$(S_o f)_{\text{ac}} = \frac{\pi D_A^2}{2\rho v_s} D[E(k)] |2k| (N_{\text{ac}} + 1) [f(-k) - f(k)] \quad (9)$$

where $D_A = 5$ eV is the deformation potential for acoustic phonons [2], $\rho = 3 \times 10^{-15}$ kg m⁻³ is the mass density of the CN [9], and $v_s = 21.1 \times 10^3$ m s⁻¹ is the velocity of sound [8].² Acoustic phonons have an energy $\hbar\omega_{\text{ac}} = \hbar v_s \beta$, where $\beta = |k - k'|$ is the phonon momentum [41].

2) *Optical Phonons*: The collision integral for optical phonons can be expressed as

$$(S_o f)_{\text{op}} = \frac{\pi D_{\text{op}}^2}{2\rho\omega_{\text{op}}} (N_{\text{op}} + 1) \times \left\{ D[E^+(k)] [1 - f(k)] \sum_{k^+} f(k^+) - D[E^-(k)] f(k) \sum_{k^-} [1 - f(k^-)] \right\} \quad (10)$$

where $D_{\text{op}} = 12.8 \times 10^{10}$ eV m⁻¹ is the deformation potential for optical phonons, which have an energy of $\hbar\omega_{\text{op}} = 200$ meV [2]. The values $f(k^\pm)$ refer to the electron distribution function for those states with an energy $\hbar\omega_{\text{op}}$ higher and lower than the state k , with $E^\pm = E(k) \pm \hbar\omega_{\text{op}}$. The summations in (10) are taken over all such allowed states k^\pm [10].

3) *Substrate Surface Polar Phonons (SPP)*: The collision integral arising from the ν th phonon mode of the substrate can be written as

$$(S_o f)_{\text{spp},\nu} = F_{\text{spp},\nu}^2 \times P_{\text{spp},\nu} \times (N_{\text{spp},\nu} + 1) \times \left\{ D[E^+(k)] [1 - f(k)] \sum_{k^+} f(k^+) - D[E^-(k)] f(k) \sum_{k^-} [1 - f(k^-)] \right\} \quad (11)$$

where the symbols are as follows: $F_{\text{spp},\nu}^2$ is the Fröhlich coupling of the ν th surface phonon mode, given in [15] as $F_{\text{spp},\nu}^2 =$

²The values of the acoustic and optical deformation potentials D_A and D_{op} appearing in (9) and (10) have been taken from [2], because the low- and high-bias mean-free paths computed from them were shown to be consistent with the experiments in the same paper; specifically, the experimental mean-free paths were found to lie within the upper bounds determined by D_A and D_{op} , which is to be expected since the experiments would include additional (above and beyond native) sources of scattering.

$\frac{\hbar\omega_{\text{spp},\nu}}{2\pi\varepsilon_0} \left(\frac{1}{\varepsilon^\infty+1} - \frac{1}{\varepsilon^0+1} \right)$, where ε^0 and ε^∞ are the low- and high-frequency dielectric constants of the polar substrate, and ε_0 is the vacuum permittivity; d is the tube diameter; $P_{\text{spp},\nu}$ is indicative of the strength of the polarization field due to the substrate phonons at a distance s away from the substrate, given by

$$P_{\text{spp},\nu} = \frac{4\pi^2 q^2 e^{-2sq_z}}{\hbar dq_z \sqrt{2\pi} (d+2s) q_z} \quad (12)$$

where s is the separation of the surface of the tube from the substrate and is set to 0.35 nm, as given by the van der Waals interaction [15], and $\hbar q_z$ is the electron momentum transfer along the tube axis, determined from [11], [15]

$$\hbar v_F q_z = \{ \hbar\omega_{\text{spp},\nu} (2\Delta + \hbar\omega_{\text{spp},\nu}) \}^{1/2} \quad (13)$$

with $v_F \approx 10^8$ cm s⁻¹ being the Fermi velocity and $2\Delta \approx 0.9/d$ eV. The values for the phonon energies and the dielectric constants of the polar substrates are taken from [27] and are listed in Table I.

B. Linearized Collision Integrals

The small-signal form of the collision integrals can be obtained in a manner similar to the linearization of the BTE outlined in Section II-A by inserting the ansatz $f = \bar{f} + \tilde{f} e^{j\omega t}$ into the full expressions (9)–(11) for the collision integrals and retaining terms to linear order in \tilde{f} . For each type of scattering, the results are as follows:

$$S_o \{ \tilde{f}, \bar{f} \}_{\text{ac}} = \frac{\pi D_A^2}{2\rho v_s} D [E(k)] |2k| (N_{\text{ac}} + 1) \left[\tilde{f}(-k) - \tilde{f}(k) \right] \quad (14)$$

$$S_o \{ \tilde{f}, \bar{f} \}_{\text{op}} = \frac{\pi D_{\text{op}}^2}{2\rho\omega_{\text{op}}} (N_{\text{op}} + 1) \times \left\{ D [E^+(k)] \sum_{k^+} [1 - \bar{f}(k)] \tilde{f}(k^+) - \bar{f}(k^+) \tilde{f}(k) - D [E^-(k)] \sum_{k^-} [1 - \bar{f}(k^-)] \tilde{f}(k^-) - \bar{f}(k^-) \tilde{f}(k^-) \right\} \quad (15)$$

and

$$S_o \{ \tilde{f}, \bar{f} \}_{\text{spp},\nu} = F_{\text{spp},\nu}^2 \times P_{\text{spp},\nu} \times (N_{\text{spp},\nu} + 1) \times \left\{ D [E^+(k)] \sum_{k^+} [1 - \bar{f}(k)] \tilde{f}(k^+) - \bar{f}(k^+) \tilde{f}(k) - D [E^-(k)] \sum_{k^-} [1 - \bar{f}(k^-)] \tilde{f}(k^-) - \bar{f}(k^-) \tilde{f}(k^-) \right\}. \quad (16)$$

REFERENCES

- [1] C. Rutherglen, D. Jain, and P. Burke, "Nanotube electronics for radiofrequency applications," *Nat. Nano*, vol. 4, no. 12, pp. 811–819, 2009.
- [2] J. Y. Park, S. Rosenblatt, Y. Yaish, V. Sazonova, H. Ustunel, S. Braig, T. A. Arias, P. W. Brouwer, and P. L. McEuen, "Electron-phonon scattering in metallic single-walled carbon nanotubes," *Nano Lett.*, vol. 4, no. 3, pp. 517–520, 2004.
- [3] T. Dürkop, S. A. Getty, E. Cobas, and M. S. Fuhrer, "Extraordinary mobility in semiconducting carbon nanotubes," *Nano Lett.*, vol. 4, no. 1, pp. 35–39, 2004.
- [4] X. Zhou, J. Y. Park, S. Huang, J. Liu, and P. L. McEuen, "Band structure, phonon scattering, and the performance limit of single-walled carbon nanotube transistors," *Phys. Rev. Lett.*, vol. 95, no. 14, pp. 146805–1–146805-4, 2005.
- [5] V. Perebeinos, J. Tersoff, and P. Avouris, "Electron-phonon interaction and transport in semiconducting carbon nanotubes," *Phys. Rev. Lett.*, vol. 94, no. 8, pp. 086802-1–086802-4, 2005.
- [6] J. Guo and M. Lundstrom, "Role of phonon scattering in carbon nanotube field-effect transistors," *Appl. Phys. Lett.*, vol. 86, no. 19, pp. 193103-1–193103-3, 2005.
- [7] A. Svizhenko and M. P. Anantram, "Effect of scattering and contacts on current and electrostatics in carbon nanotubes," *Phys. Rev. B*, vol. 72, no. 8, pp. 085430-1–085430-10, 2005.
- [8] S. O. Koswatta, S. Hasan, M. S. Lundstrom, M. P. Anantram, and D. E. Nikonov, "Ballistic of nanotube field-effect transistors: Role of phonon energy and gate bias," *Appl. Phys. Lett.*, vol. 89, no. 2, pp. 23125-1–23125-3, 2006.
- [9] G. Pennington, N. Goldsman, A. Akturk, and A. E. Wickenden, "Deformation potential carrier-phonon scattering in semiconducting carbon nanotube transistors," *Appl. Phys. Lett.*, vol. 90, no. 6, pp. 62110-1–62110-3, 2007.
- [10] N. Paydavosi, A. U. Alam, S. Ahmed, K. D. Holland, J. P. Rebstock, and M. Vaidyanathan, "RF performance potential of array-based carbon-nanotube transistors—Part I: Intrinsic results," *IEEE Trans. Electron Devices*, vol. 58, no. 7, pp. 1928–1940, Jul. 2011.
- [11] A. G. Petrov and S. V. Rotkin, "Energy relaxation of hot carriers in single-wall carbon nanotubes by surface optical phonons of the substrate," *JETP Lett.*, vol. 84, no. 3, pp. 156–160, 2006.
- [12] V. Perebeinos, J. Tersoff, and P. Avouris, "Mobility in semiconducting carbon nanotubes at finite carrier density," *Nano Lett.*, vol. 6, no. 2, pp. 205–208, 2006.
- [13] B. Chandra, V. Perebeinos, S. Berciaud, J. Katoch, M. Ishigami, P. Kim, T. F. Heinz, and J. Hone, "Low bias electron scattering in structure-identified single wall carbon nanotubes: Role of substrate polar phonons," *Phys. Rev. Lett.*, vol. 107, no. 14, pp. 146601-1–146601-4, 2011.
- [14] G. D. Mahan, "Surface polaritons and the theory of image charges," *Phys. Rev. B*, vol. 5, no. 2, pp. 739–744, 1972.
- [15] V. Perebeinos, S. V. Rotkin, A. G. Petrov, and P. Avouris, "The effects of substrate phonon mode scattering on transport in carbon nanotubes," *Nano Lett.*, vol. 9, no. 1, pp. 312–316, 2009.
- [16] N. Paydavosi, J. P. Rebstock, K. D. Holland, S. Ahmed, A. U. Alam, and M. Vaidyanathan, "RF performance potential of array-based carbon-nanotube transistors—Part II: Extrinsic results," *IEEE Trans. Electron Devices*, vol. 58, no. 7, pp. 1941–1951, Jul. 2011.
- [17] *COMSOL Multiphysics Version 3.5 a*. COMSOL, Inc., Stockholm, Sweden, 2008.
- [18] R. Ludwig and G. Bogdanov, *RF Circuit Design: Theory and Applications*. 2nd ed. Upper Saddle River, NJ, USA: Prentice-Hall, 2009.
- [19] "Radio frequency and analog/mixed-signal technologies for wireless communications," International Technology Roadmap for Semiconductors, 2009 Edition. [Online]. Available: http://www.itrs.net/Links/2009ITRS/2009Chapters_2009Tables/2009_Wireless.pdf
- [20] S. Datta, *Quantum Transport: Atom to Transistor*. Cambridge, U. K.: Cambridge University Press, 2005.
- [21] S. Fratini and F. Guinea, "Substrate-limited electron dynamics in graphene," *Phys. Rev. B*, vol. 77, no. 19, pp. 195415-1–195415-6, 2008.
- [22] A. Konar, T. Fang, and D. Jena, "Effect of high-k gate dielectrics on charge transport in graphene-based field effect transistors," *Phys. Rev. B*, vol. 82, no. 11, pp. 115452-1–115452-7, 2010.
- [23] Z. Y. Ong and M. V. Fischetti, "Theory of interfacial plasmon-phonon scattering in supported graphene," *Phys. Rev. B*, vol. 86, no. 16, pp. 165422-1–165422-15, 2012.
- [24] Z. Y. Ong and M. V. Fischetti, "Erratum: Theory of interfacial plasmon-phonon scattering in supported graphene," *Phys. Rev. B*, vol. 86, no. 19, pp. 199904-1–199904-2, 2012.
- [25] Z. Y. Ong and M. V. Fischetti, "Top oxide thickness dependence of remote phonon and charged impurity scattering in top-gated graphene," *Appl. Phys. Lett.*, vol. 102, no. 18, pp. 183506-1–183506-4, 2013.

- [26] F. Wang, D. J. Cho, B. Kessler, J. Deslippe, P. J. Schuck, S. G. Louie, A. Zettl, T. F. Heinz, and Y. R. Shen, "Observation of excitons in one-dimensional metallic single-walled carbon nanotubes," *Phys. Rev. Lett.*, vol. 99, no. 22, pp. 227401-1–227401-4, 2007.
- [27] M. V. Fischetti, D. A. Neumayer, and E. A. Cartier, "Effective electron mobility in Si inversion layers in metal-oxide-semiconductor systems with a high-k insulator: The role of remote phonon scattering," *J. Appl. Phys.*, vol. 90, no. 9, pp. 4587–4608, 2001.
- [28] N. Paydavosi, K. D. Holland, M. M. Zargham, and M. Vaidyanathan, "Understanding the frequency- and time-dependent behavior of ballistic carbon-nanotube transistors," *IEEE Trans. Nanotechnol.*, vol. 8, no. 2, pp. 234–244, Mar. 2009.
- [29] N. Paydavosi, M. M. Zargham, K. D. Holland, C. M. Dublanko, and M. Vaidyanathan, "Non-quasi-static effects and the role of kinetic inductance in ballistic carbon-nanotube transistors," *IEEE Trans. Nanotechnol.*, vol. 9, no. 4, pp. 449–463, 2010.
- [30] D. Kienle, M. Vaidyanathan, and F. Léonard, "Self-consistent ac quantum transport using nonequilibrium Green functions," *Phys. Rev. B*, vol. 81, no. 11, pp. 115455-1–115455-10, 2010.
- [31] D. Kienle and F. Léonard, "Terahertz response of carbon nanotube transistors," *Phys. Rev. Lett.*, vol. 103, no. 2, pp. 026601-1–026601-4, 2009.
- [32] K. Holland, N. Paydavosi, and M. Vaidyanathan, "Self-consistent simulation of array-based CNFETs: Impact of tube pitch on RF performance," in *Proc. 14th Int. Wireless Commun. Expo.*, Oct. 2010, pp. 291–294.
- [33] L. Liao, Y. C. Lin, M. Bao, R. Cheng, J. Bai, Y. Liu, Y. Qu, K. L. Wang, Y. Huang, and X. Duan, "High-speed graphene transistors with a self-aligned nanowire gate," *Nature*, vol. 467, pp. 305–308, 2010.
- [34] S. Lee, B. Jagannathan, S. Narasimha, A. Chou, N. Zamdmer, J. Johnson, R. Williams, L. Wagner, J. Kim, J. Plouchart, J. Pekarik, S. Springer, and G. Freeman, "Record RF performance of 45-nm SOI CMOS technology," in *Proc. IEEE Int. Electron. Devices Meet.*, Dec. 2007, pp. 255–258.
- [35] D. H. Kim and J. A. del Alamo, "30-nm InAs PHEMTs with $f_T = 644$ GHz and $f_{max} = 681$ GHz," *IEEE Electron. Device Lett.*, vol. 31, no. 8, pp. 806–808, Aug. 2010.
- [36] W. Hafez, W. Snodgrass, and M. Feng, "12.5 nm base pseudomorphic heterojunction bipolar transistors achieving $f_T = 710$ GHz and $f_{MAX} = 340$ GHz," *Appl. Phys. Lett.*, vol. 87, no. 25, pp. 252109-1–252109-3, 2005.
- [37] M. S. Gupta, "Power gain in feedback amplifiers, a classic revisited," *IEEE Trans. Microw. Theory Tech.*, vol. 40, no. 5, pp. 864–879, May 1992.
- [38] L. C. Castro and D. L. Pulfrey, "Extrapolated f_{max} for carbon nanotube field-effect transistors," *Nanotechnology*, vol. 17, no. 1, pp. 300–304, 2006.
- [39] M. Vaidyanathan and D. L. Pulfrey, "Extrapolated f_{max} of heterojunction bipolar transistors," *IEEE Trans. Electron. Devices*, vol. 46, no. 2, pp. 301–309, Feb. 1999.
- [40] H. Dai, A. Javey, E. Pop, D. Mann, W. Kim, and Y. Lu, "Electrical transport properties and field effect transistors of carbon nanotubes," *Nano*, vol. 1, no. 1, pp. 1–13, 2006.
- [41] M. Lundstrom, *Fundamentals of Carrier Transport*. 2nd ed. New York, NY, USA: Cambridge University Press, 2000.



Sabbir Ahmed received the B.Sc. and M.Sc. degrees in electrical and electronic engineering (EEE) from the Bangladesh University of Engineering and Technology (BUET), Dhaka, Bangladesh, in 2005 and 2007, respectively. In 2008, he joined the University of Alberta, Edmonton, AB, Canada, where he is currently working towards the Ph.D. degree, on leave from BUET.

From 2005 to 2008, he was a Lecturer with the Department of EEE of BUET. His research interests include the theory, modeling, and simulation of nanoscale electronic devices, with an emphasis on the high-frequency and circuit-level performance of III–V high-electron-mobility transistors, carbon-based transistors and solar cell devices.

Mr. Ahmed received the F. S. Chia Doctoral Scholarship in 2008 and 2009, and the Queen Elizabeth II Graduate Scholarship in 2010, 2011, and 2012 at the University of Alberta.



Navid Paydavosi received the B.A.Sc. degree in electrical engineering from Shahid Beheshti University, Tehran, Iran, in 2005, and the Ph.D. degree in electrical engineering from the University of Alberta, Edmonton, AB, Canada, in 2011.

He is currently a Postdoctoral Scholar with the BSIM Group in the University of California, Berkeley, CA, USA. His research interests are in the theory and modeling of future alternatives to ordinary silicon transistors, including carbon-based and III–V high-electron-mobility devices, with an emphasis on the high-frequency characteristics relevant for RF applications, such as the extrinsic cutoff frequency, the attainable power gain, the unity-power-gain frequency, and linearity.

Dr. Paydavosi received the Queen Elizabeth II Graduate Scholarship for September 2009 and January 2010, and two Tuition Supplement Awards in September 2006 and April 2007 from the University of Alberta.



Ahsan Ul Alam received the B.Sc. and the M.Sc. degrees in electrical and electronic engineering from the Bangladesh University of Engineering and Technology (BUET), Dhaka, Bangladesh, in 2005 and 2007, respectively. Currently, he is on study leave from BUET, working toward the Ph.D. degree at the University of Alberta, Edmonton, AB, Canada.

From 2005 to 2008, he was a Lecturer at BUET, teaching courses and performing research in the area of semiconductor devices. His research interests include the theory and modeling of semiconductor devices, where he has worked on topics ranging from the study of spin transport in carbon-based devices to the modeling of high-frequency distortion for wireless applications.

Mr. Alam received the Kintar-ul Huq Lashkar Gold Medal from BUET for securing the top position in his undergraduate studies. He also received the F. S. Chia Ph.D. Scholarship in the first two years and the Queen Elizabeth II Graduate Scholarship in the third, fourth, fifth, and sixth year of his Ph.D. studies at the University of Alberta.



Kyle David Holland received the B.Sc. degree in engineering physics (nanoengineering option) from the University of Alberta, Edmonton, AB, Canada, in 2009, where he is currently working toward the Ph.D. degree in electrical engineering.

His research interests include quantum simulation of carbon-based nanoelectronics, with an emphasis on modeling the high-frequency performance of graphene devices.

Mr. Holland currently holds an NSERC Alexander Graham Bell Canada Graduate Scholarship and an Alberta Innovates Graduate Student Scholarship, and he was a recipient of the Ralph Steinhauer Award of Distinction.



Diego Kienle received the B.S. (*Vordiplom*) and the M.S. (*Diplom*) degrees from the University of Bayreuth, Bayreuth, Germany, and the Ph.D. (*Dr.rer.nat.*) degree from the Research Center Jülich and the University of Saarland, Saarbrücken, Germany, all in theoretical physics.

After Postdoctoral appointments with the Electrical and Computer Engineering Department at Purdue University, West Lafayette, IN, USA, and the Material Science Department at Sandia National Laboratories, CA, USA, he is currently with the Institute of

Theoretical Physics at the University of Bayreuth. His research interests include the formal theory, modeling, and simulation of ac quantum electronic transport in nanoscale materials and devices with focus on the understanding of the quantum dynamic processes in low-dimensional materials and their potential application in solid-state based terahertz devices. His past research interests were in the theory and modeling of complex fluids by means of Brownian dynamics with focus on many-body hydrodynamic interaction effects in diluted polymer solutions.

Mani Vaidyanathan (S'95–M'99) received the Ph.D. degree in electrical engineering from the University of British Columbia, Vancouver, BC, Canada, in 1999.

He is currently an Associate Professor with the Department of Electrical and Computer Engineering at the University of Alberta, Edmonton, AB, Canada. His research interests include the modeling, simulation, and understanding of electronic devices for future technologies, with a present focus on the radio-frequency performance of carbon-nanotube and graphene-based devices.

Dr. Vaidyanathan is a recipient of the University of Alberta's Provost's Award and the University of Alberta's Alexander Rutherford Award, both for excellence in teaching.